

Scattered Dose Calculations and Measurements in a Life-Like Mouse Phantom

David Welch,^a Leah Turner,^a Michael Speiser,^b Gerhard Randers-Pehrson^a and David J. Brenner^{a,1}

^a Center for Radiological Research, Columbia University, New York, New York; and ^b Englewood Hospital and Medical Center, Englewood, New Jersey

Welch, D., Turner, L., Speiser, M., Randers-Pehrson, G. and Brenner, D. J. Scattered Dose Calculations and Measurements in a Life-Like Mouse Phantom. *Radiat. Res.* **187**, 433–442 (2017).

Anatomically accurate phantoms are useful tools for radiation dosimetry studies. In this work, we demonstrate the construction of a new generation of life-like mouse phantoms in which the methods have been generalized to be applicable to the fabrication of any small animal. The mouse phantoms, with built-in density inhomogeneity, exhibit different scattering behavior dependent on where the radiation is delivered. Computer models of the mouse phantoms and a small animal irradiation platform were devised in Monte Carlo N-Particle code (MCNP). A baseline test replicating the irradiation system in a computational model shows minimal differences from experimental results from 50 Gy down to 0.1 Gy. We observe excellent agreement between scattered dose measurements and simulation results from X-ray irradiations focused at either the lung or the abdomen within our phantoms. This study demonstrates the utility of our mouse phantoms as measurement tools with the goal of using our phantoms to verify complex computational models. © 2017 by Radiation Research Society

INTRODUCTION

Small animal models have become essential tools for radiation biology research (1). These models, primarily of mice, offer well-known genetic profiles which make them ideal as experimental test beds. One specific research area utilizing these small animal models is radiotherapy. The past twenty years have seen a number of technological advancements in the delivery of radiation with targeted beams; however, many of those systems and methods were never validated on animal models due to the absence of equipment capable of replicating human sized experiments on small animals. Thus, recent research has pushed to create

systems which mimic the capabilities of human radiotherapy on small animal models. A number of experimental small animal irradiation systems have been developed in the past ten years, with some even becoming commercially available (2–4). These systems have high-resolution imaging capabilities, technically precise robotic movements, and energies scaled to match the small animal geometries. Concurrent to the rise in popularity of these irradiation systems has been a call for accurate and standardized dosimetry within small animal models (5, 6).

Radiation dose calculation can be performed computationally, i.e., with a mathematical model of a system, or with a physical measurement using devices such as thermoluminescent dosimeters (TLD), MOSFET dosimeters or radiation sensitive film (7). Computational models have grown in power over the past fifty years largely thanks to the increased availability and power of computers (8). These computerized analysis techniques create a computational phantom which defines the geometry analyzed in the model. The methods of representing computational phantom geometry have evolved from simply defining shapes with quadratic equations, to voxel based representations, to the current generation which uses boundary representation with non-uniform rational B-splines or polygonal meshes. The most advanced models also include capabilities to deform the model over time during a simulation. Most of the advancements in computational phantom technology first focused on anthropomorphic phantoms. Small animal computational model development has since followed the same trajectory with equation based models (9, 10) and more recently advanced voxel based models (11–15).

The physical measurement of dose utilizes solid materials to create a phantom and gathers data from strategically placed dosimeters, and like the computational models, the level of complexity has increased over time. Simple physical phantoms, often just slabs of tissue equivalent material, are still critical for standardization procedures; however, anthropomorphic phantoms, which mimic the human body in shape and heterogeneous density distribution, receive significant usage especially in analysis of dose delivery to specific organs (16–20). The widespread usage of small animal models has spurred development of

¹ Address for correspondence: Center for Radiological Research, Columbia University, 630 W. 168th St., New York, NY 10032; email: djb3@cumc.columbia.edu.

physical phantoms of mice as well. Simple mouse phantoms, which are often no more than a tube with slots for the insertion of a detector, are prevalent for dosimetry (3, 5, 6, 21). The rise in popularity and capability of rapid prototyping tools, such as 3D printers and computer controlled milling machines, has allowed for a new generation of physical mouse phantoms with intricate features that closely mimic the animals they represent. Multiple mouse phantoms have been created using 3D printing, but they are often homogenous (22) and any heterogeneities that can be created are limited to variations in optical response (23, 24). Bache *et al.* employed 3D printing to produce molds for optical dosimeters, which had the same anatomical shape as small sections of a mouse, but those dosimeters also lacked structures to mimic bones and other regions of density inhomogeneity (25). In our previous work, we demonstrated the construction of anatomically accurate mouse phantoms with heterogeneous internal structures including bone and lung equivalent regions (26). To the best of our knowledge, our fabricated phantoms remain the most accurate representations of mouse anatomy for radiation dosimetry experiments.

With the work presented here we investigate the crucial factor in the application of both computational and physical phantoms – verification that these models are, in fact, good representations of the phenomenon imitated. In the comprehensive review of computational phantoms by Xu, it is noted that “experimental work involving a whole-body physical phantom is still needed to verify the calculations especially when involving complex irradiation conditions” (8). Furthermore, initial modeling work of small animal radiotherapy research platforms emphasized that “tissue heterogeneity, most notably bone attenuation” is very important to dosimetry considering the unique energies and delivery processes with these machines (27). The topic of inhomogeneity and its effect on dose assessment has been discussed by other groups as well (28, 29). We are uniquely positioned to explore this problem because of our ability to produce anatomically accurate mouse phantoms with heterogeneous internal structures. Previous related work with small animal irradiations have either been purely computational (30) or made comparisons using simple phantoms (31). This work investigates dose distributions, specifically scattered dose outside the beam target region, from specialized animal irradiators using both a complex physical phantom and an accompanying complex computational phantom to generate new insight into small animal irradiation investigations.

METHODS

Phantom Fabrication Process

With our previous work in the construction of mouse phantoms we based our design off of the publicly available Digimouse model (26). However, the Digimouse utilized a mouse which was sacrificed and bound to a jig to hold it in place throughout multiple imaging

modalities to aid in co-localization of points for accurate segmentation (32). While this setup was helpful for segmentation of the many different regions, it produced a mouse model which was in an unnatural position – the model has legs spread out and the stomach and back are compressed and flattened, this is in contrast to a more common relaxed position with limbs close to the body. For this work we chose to model our phantoms off of a living mouse, and therefore a more natural position. We achieved this by imaging an adult wildtype mouse under anesthesia using a Quantum FX micro CT Imaging System (PerkinElmer, Waltham, MA). The scan generated 3D tomography data with a voxel size of 236 μm . While the micro CT is capable of imaging at a higher resolution, this was the maximum resolution possible while still capturing the entire mouse in a single scan. The scan data was exported as 512 DICOM images.

Segmentation of the CT data was performed using 3D-Doctor software (Able Software Corp, Lexington, MA). The DICOM images were imported into 3D-Doctor and regions of bone, lung and tissue (the remaining volume of the mouse) were selected using a combination of auto-segmentation features and manual adjustments. External equipment, such as the imaging couch and the anesthesia nose cap, were easily excluded during the segmentation procedure for complete isolation of the segmented mouse model. A three-dimensional rendering of the segmented model showing regions of bone and lung within a mouse volume is shown in Fig. 1. Segmentation data was exported in three separate XYZ files, one each for lung, bone, and tissue. Each XYZ file contained the coordinates within the volume which correspond to each segmented region. These files were combined in MATLAB (Mathworks, Natick, MA) to create a three-dimensional array of the segmented mouse.

With the segmented mouse model imported into MATLAB the construction of the mouse phantom was identical to our previously described procedure (26). Briefly, slices from the segmented model are extracted and combined into a single two-dimensional image. The image is used to generate g-code which defines the cutting path for a computer controlled milling machine. A slab of 2 mm thick tissue equivalent plastic (model no. 452-202 Muscle, Gammex Inc., Middleton, WI) is milled to create regions for the insertion of lung or bone equivalent material. We mimic lung tissue with a urethane rubber mixture using polystyrene microbeads to decrease the density. Bone equivalent material is an epoxy resin with silicon dioxide and calcium carbonate added. All materials have a composition to match the mass density, mass attenuation coefficients and mass energy absorption coefficients within the diagnostic energy range (33, 34). The individual phantom slices are removed from the slab and each region is filled as appropriate. The phantoms are assembled with alignment rods, also made of tissue equivalent plastic, which extend through the model perpendicular to the slice plane.

Newly Constructed Mouse Phantom

Two mouse phantoms based off of the CT scan of a single living mouse are shown in Fig. 1. The phantom with coronal slices contains 11 pieces while the phantom with sagittal slices consists of 13. The coronal phantom is 9 cm \times 2.6 cm \times 2.2 cm (length \times width \times height) with a mass of 30.8 grams. The sagittal phantom is 9 cm \times 2.6 cm \times 2.5 cm with a mass of 31.7 grams. A photograph of a slice of the coronal phantom is shown in Fig. 2C. Comparing the image of the fabricated slice with the segmented model it was designed with, shown in Fig. 2D, demonstrates our ability to closely mimic the precise geometry throughout the phantom.

Irradiation Procedure

The Small Animal Radiation Research Platform (SARRP) (Xstrahl Ltd., Surrey, UK) enables state-of-the-art image-guided radiotherapy research to be performed on small animal models (35). The SARRP consists of a 220 kVp X-ray tube mounted on a rotating gantry. The tube has a tungsten target and an intrinsic filtration of 0.8 mm

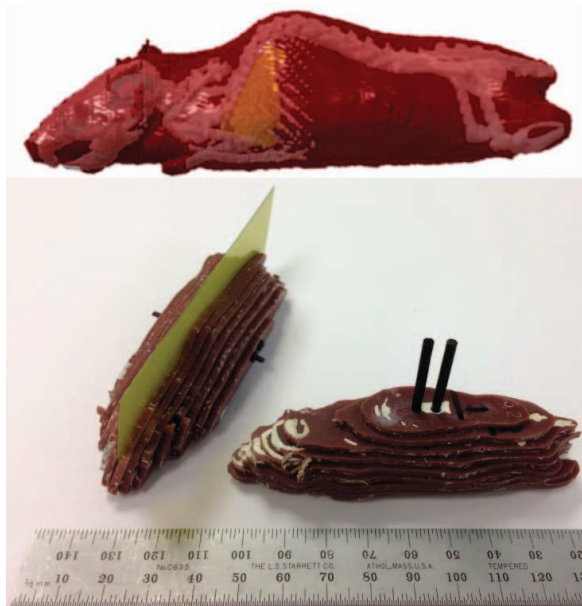


FIG. 1. A 3D rendering of the segmented mouse model created with 3D-Doctor is shown at the top of the figure. The model contains regions of bone (white), lung (yellow), and the remaining volume of the mouse (red). The two mouse phantoms created in the likeness of the living mouse are pictured at the bottom. The phantom composed of slices in the sagittal plane is shown with a piece of radiochromic film inserted. The black rods which extend through each of the phantoms are tissue equivalent plastic and maintain alignment of the assembled phantoms during experimentation.

beryllium; an additional 0.15 mm copper filter is used during irradiations. Various collimator nozzles are available to create beam sizes, denoted as the field size at isocenter, of 10×10 mm square, 5×5 mm square, 3×3 mm square, 9×3 mm rectangular and 0.5 mm and

1.0 mm diameter circular at 35 cm from the source. Computer-controlled robotic translation and rotation stages are used to move a carbon fiber bed to position the animal in relationship to the focal spot. The SARRP is equipped with cone-beam CT (CBCT) image guidance and the user can select a target within the acquired image as the focal point of the beam for subsequent irradiation.

We irradiated Gafchromic EBT3 radiochromic film (Ashland, Covington, KY) to measure and characterize the SARRP treatment beam. The film has a total thickness of $278 \mu\text{m}$ made up of a $28 \mu\text{m}$ active region with a $125 \mu\text{m}$ polyester base coating on either side (36). Holes were drilled through the film to allow placement between slices in a secured position using the alignment rods in each phantom. Two different targeted irradiations are typically performed in our lab using the SARRP and thus were the focus of this study. The first is a lung irradiation using the 3×3 mm square collimator nozzle positioned to deliver a beam through the dorsal side of the animal to the lung. Lung irradiations were performed using the phantom made of coronal slices with film positioned between the fifth and sixth slice counting from the ventral side (1 cm from the bottom of the phantom), thus the film was perpendicular to the beam position. The second irradiation procedure is an abdominal irradiation using the 5×5 mm square collimator nozzle positioned to deliver a beam to the center of abdomen through the side of animal. Abdominal irradiations were performed using the phantom comprised of sagittal slices and the film was between the sixth and seventh slice from the right side. All irradiations in this study were performed at 220 kVp and 13 mA.

Film Dosimetry

Gafchromic films were scanned as 48 bit RGB TIFF images using an Epson Perfection V700 Photo flatbed scanner (Epson, Suwa, NGN, Japan). The image files were processed using custom software developed by Alves *et al.* (37) that improves on multichannel methods (38) by using robust optimization for dose calculation. Calibration doses for the films were administered using the 10×10 mm square collimator nozzle on the SARRP with pieces of EBT3 film sandwiched between two slabs of 5 mm thick tissue equivalent plastic (model no. 452-205 Muscle, Gammex Inc., Middleton, WI). The

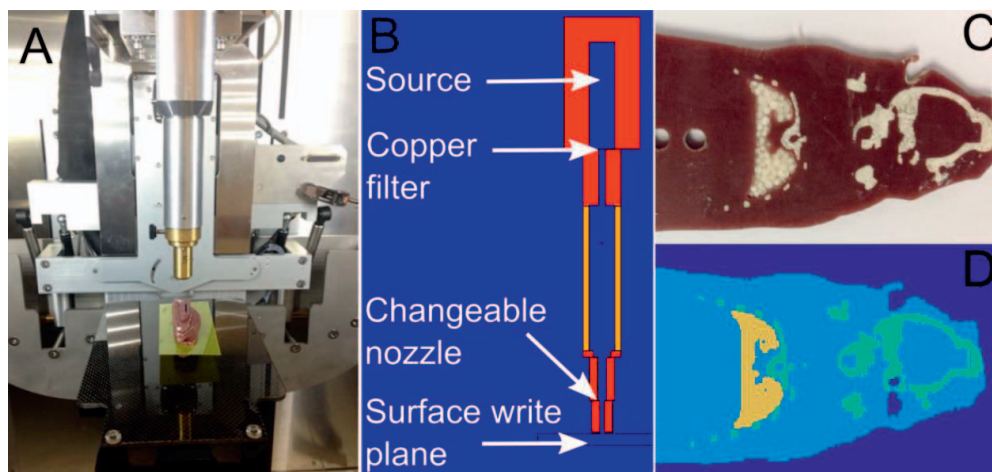


FIG. 2. Panel A: The interior of the SARRP is pictured with a mouse phantom positioned below the collimator. The mouse phantom rests on a robotically controlled carbon fiber couch which is moved in relationship to the collimator allowing for targeting of specific internal structures identified with a CBCT scan performed prior to irradiation. Panel B: A screenshot of the collimation unit as it was defined in MCNP. A surface write plane was used to record particles as they exited the nozzle; this surface could be employed in later simulations as a source. Panel C: A photograph of a single layer of the physical phantom made up of coronal slices clearly shows regions of bone and lung equivalent material within tissue equivalent plastic. Panel D: An image of the model used to create both the physical and computational phantoms is shown. Minor differences exist between the physical phantom and the computational phantom due to the fabrication constraints.

SARRP, which was calibrated using an ion chamber, had a dose rate of 0.039 Gy/s when using the 10×10 collimator.

MCNP Modelling

MCNP6.1 is a general-purpose Monte Carlo N-Particle code used for neutron, photon and electron transport in three dimensional problems (39). A model of the SARRP was generated in MCNP based on specifications supplied by the manufacturer and found in previously published work modeling the system (27). An overview of the geometry modeled is shown in Fig. 2A and B. We chose to model the source particles for the X-ray tube as the spectrum of photons produced off of the tungsten target (including the intrinsic Be filtration) as calculated using Spekcalc (40). The additional copper filtration present in the SARRP was included in the MCNP modeled geometry. To reduce overall computation time in subsequent calculations we made use of the surface source file writing capabilities in MCNP6 to save the properties of all particles exiting the collimation structure. Many of the original source particles were either filtered out or did not make it through a given collimator opening so this allowed for only those relevant particles to be tracked in later simulations. A separate surface source file was produced for each collimator nozzle size needed. The surface source could be maneuvered independently in later simulations to allow the beam to be aimed at any point. This modeling strategy breaks up the total simulation because the interactions upstream of the end of the nozzle were not repeated each time, therefore reducing total computation time.

All MCNP simulations were performed using a Dell Latitude E5430 computer with an Intel Core i5-3340 CPU at 2.7 GHz. Each simulation used 1×10^{10} starting particles that produced estimated relative error values, defined as the estimated standard deviation of the mean divided by the estimated mean, of less than 0.05. Rectangular mesh tallies used the type 3 tally to score energy deposition data in which the energy deposited per unit volume from all particles was included. The tally geometry was defined to coincide with the layer of radiochromic film and thus every tally would have identical density and volume for a given experimental setup. We used the gridconv program included with MCNP to format the normalized output data as text which could be input to MATLAB and post processed. The normalized MCNP outputs were scaled to a nominal dose of 50 Gy to allow for easy comparison of data.

MCNP Model of Mouse Phantoms

Models of our mouse phantoms were input into MCNP using the lattice repeated structure capability. The lattice was specified as hexahedra with element dimensions of $236 \mu\text{m} \times 236 \mu\text{m} \times 2 \text{mm}$, which corresponds to the voxel dimensions of the original mouse CT scan and the thickness of an individual slice. The lattice for the coronal phantom was $426 \times 141 \times 11$ elements and the sagittal phantom was $151 \times 426 \times 13$ elements; each lattice was identical to the segmented model used to manufacture the physical phantoms. Every element of the array was assigned different material properties which correspond to the elemental compositions and density of the tissue equivalent, bone equivalent, and lung equivalent materials used to manufacture our mouse phantoms as well as the air surrounding the model. The lattice could be split and a volume of Gafchromic film inserted into the simulation in an identical position as used in the irradiation. The carbon fiber couch to support the phantom was also included in simulations.

An example slice of the MCNP model is shown in Fig. 2D along with the corresponding slice from the physical phantom in Fig. 2C. While the simulated model contains minor features that were unachievable in the physical phantoms due to fabrication limitations, overall we observe good agreement between the physical and mathematical models.

Baseline Irradiation

An irradiation setup consisting of EBT3 film sandwiched between two slabs of 5 mm thick tissue equivalent plastic was used to obtain baseline measurements of scattered dose. This setup is identical to the setup used for taking dose standards for film calibration. Baseline measurements were taken with both the 5×5 mm square and 3×3 mm square collimators with a nominal dose of 50 Gy delivered. The irradiation geometry was replicated in MCNP to obtain baseline levels of scattered dose in simulations with each collimator.

RESULTS

Verification of SARRP Modeling in MCNP

To verify that our MCNP simulation is an accurate model we compared baseline irradiation dose profiles using film and MCNP. This simple geometry was compared using both the 3×3 mm and 5×5 mm collimators. The total dose deposited in $200 \mu\text{m}$ wide bins across the center of each beam target area is plotted in Figs. 3 and 4. In both the 3×3 mm and 5×5 mm plots there is a very close agreement between the simulation and film results down to approximately 0.1 Gy. When the film and MCNP doses diverge the MCNP simulation dose result continues to decrease steadily while the film dose shows more variability. This variability is likely due to the film surpassing its minimum sensitivity, stated as about 0.1 Gy by the manufacturer. The bin size of $200 \mu\text{m}$ was chosen to give a good resolution of the dose diminishing away from the center of the beam. However, the small bin size paired with the infrequency of particles passing far away from the collimated beam caused relative error values to increase to upwards of 0.3 at the extents of the graph and thus these measurements exhibit more inconsistency.

Comparison of EBT3 Film and MCNP for Phantom Irradiation

Two-dimensional dose map comparisons between film and MCNP using the 3×3 mm and 5×5 mm collimator are shown in Figs. 5 and 6, respectively. Each dose map is divided into a 3×3 mm or 5×5 mm grid, which is centered and aligned to the position of the beam. The results for the baseline irradiation test and simulation are shown in the left column of each figure. Dose maps for testing within a mouse phantom are shown in the right column of each figure; these dose maps are superimposed over the cross section of the mouse phantom to indicate the region where the beam was aimed. The MCNP results for each irradiation are normalized to a nominal dose of 50 Gy. The ratios of film results to MCNP results (ratio = film dose/MCNP dose) for each irradiation are shown in the bottom row of the Figs. 5 and 6.

The 3×3 mm collimator baseline results (Fig. 5, left column) show a generally good agreement with minor discrepancies highest just away from center and at the edges of the dose map. Ratios for the lung irradiation phantom experiment (Fig. 5, right column) are fairly consistent throughout the measured region, with film doses only

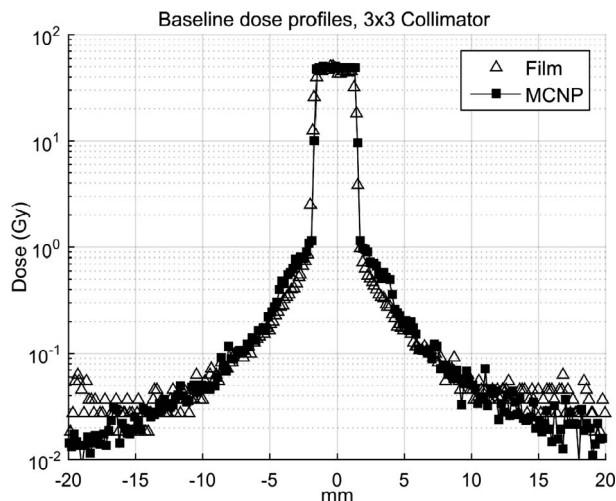


FIG. 3. Dose profiles sampled across a baseline exposure using the 3×3 mm square collimator are plotted with results from both radiochromic film and MCNP simulations. The film exposure was performed with a nominal dose of 50 Gy in the center of the beam. MCNP simulations were normalized to 50 Gy to aid in comparing results. The baseline exposure included EBT3 film sandwiched between two slabs of 5 mm thick tissue equivalent plastic used to minimize backscatter effects.

slightly higher than MCNP doses in the areas adjacent to the target region.

The 5×5 mm collimator baseline results (Fig. 6, left column) also show a good agreement across the dose map and overall appear more consistent than the 3×3 mm results. Ratios for the abdominal irradiation phantom experiment (Fig. 6, right column) show excellent agreement with minimal discrepancies. Both the measured film doses and the MCNP simulations indicate higher amounts of scattering with the 5×5 mm collimator than with the 3×3 mm collimator.

DISCUSSION

The new generation of mouse phantoms presented here are excellent models of a typical mouse used in a small animal irradiation. The phantoms are anatomically accurate with the entire mouse positioned in a natural position, an upgrade from our previously constructed phantoms. The change in phantom positioning has a significant effect on key internal features; for example, the thoracic cavity in our previous phantoms, which were based on the Digimouse model, was compressed whereas this generation reproduces a mouse with a relaxed position thus correcting the geometry of the internal organs including the lung. Inclusion of model geometry acquisition and segmentation from a micro CT scan into our fabrication procedure achieves a complete process for replicating mice for radiation dosimetry experiments. Furthermore, this process is generalized so that other small animals, such as rats, can have phantoms fabricated via the same methods.

Analysis of the scattered dose experiments performed in this work leads to a number of observations. One of the first

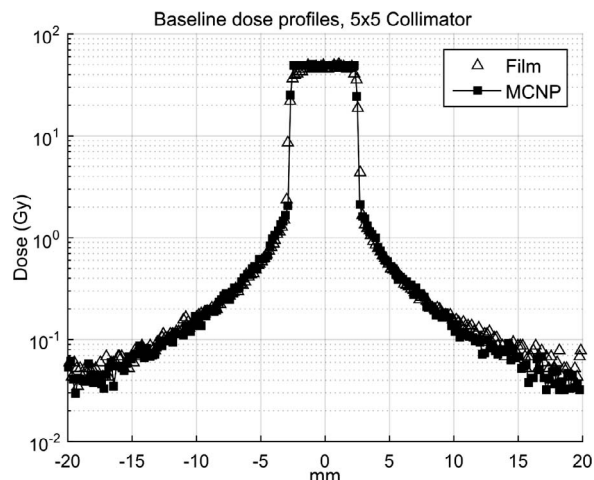


FIG. 4. Dose profiles sampled across a baseline exposure using both the 5×5 mm square collimator are plotted with results from both radiochromic film and MCNP simulations. The film exposure was performed with a nominal dose of 50 Gy in the center of the beam. MCNP simulations were normalized to 50 Gy to aid in comparing results. The baseline exposure included EBT3 film sandwiched between two slabs of 5 mm thick tissue equivalent plastic used to minimize backscatter effects.

is the very good agreement between the dose profile plots in Figs. 3 and 4. The matched profile extends from 50 Gy down to 0.1 Gy which indicates that our simulation parameters are a good representation of the physical experiment. Another observation is the differences in scattered dose between the two collimators tested. Increased extra-focal collimator scatter is observed for the 5×5 mm collimator in both experimental and simulation results. This difference is expected because of the higher probability of particles scattering out of the collimator at a large angle through the wider opening. The dose profiles in Figs. 3 and 4 also illustrate the limits of the radiochromic film used in this study. The measured film dose values approach a lower limit of about 0.1 Gy and begin to deviate from the MCNP profile at lower doses. If the film had a higher sensitivity to low doses it is likely that they would follow the simulation results over an even larger range.

Examination of the two-dimensional dose maps in Figs. 5 and 6 shows a generally good agreement between the measurements and simulations. One trend in comparing the film results with the simulation results is observation of a higher dose immediately adjacent to the targeted region in all of the film dose maps. This increase in dose is likely deceptively large due to the method of calculating dose across each 3×3 mm or 5×5 mm region on the film. The film, which was digitized with a photo scanner at 150 dpi, was likely at a slight rotational angle with respect to the pixels of the scanner. This angle, possibly as little as a couple of degrees, would rotate the target region with respect to the square analysis region and extend corners into each adjacent square. The dose in each region is calculated as the mean of the dose for all pixels within the region; this agrees with the methods of MCNP dose calculation.

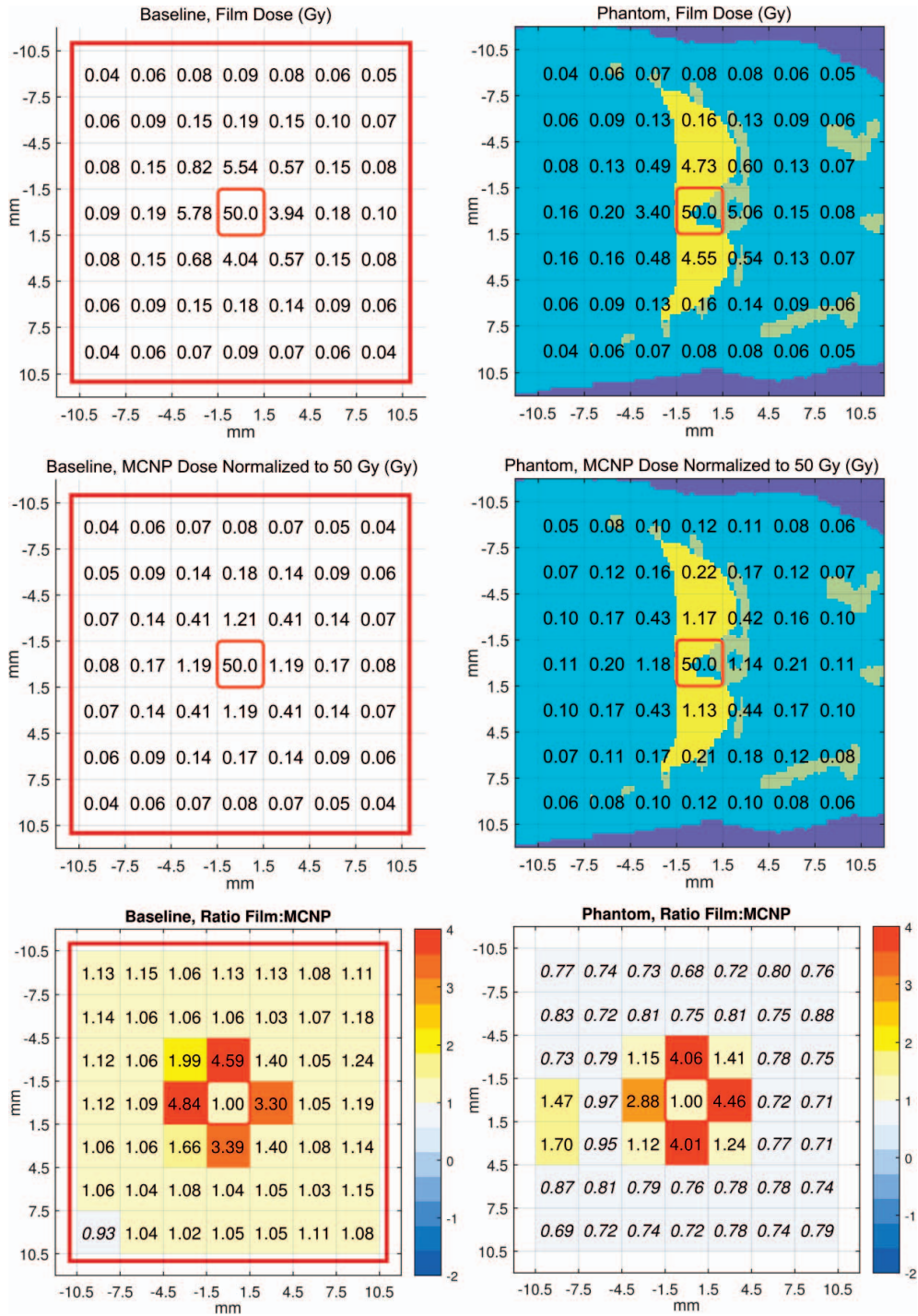


FIG. 5. Plots in the first two rows show dose maps of exposures using the 3×3 mm collimator with film results and MCNP results for both a baseline experiment and a phantom irradiation. Dose is shown normalized to a 50 Gy nominal dose delivered at the center of the beam. The 3×3 mm region highlighted at the center indicates the beam target area. The dose map for the phantom irradiations includes an underlay of the coronal sliced phantom geometry with lung regions indicated as yellow, bone as gray, tissue as light blue, and air as dark blue. The dose administered to the mouse phantom by the SARRP was aimed at the center of the lung region and delivered through the dorsal side. The bottom two plots show the ratio of film dose to MCNP dose in each of the experimental setups. Values displayed in the film and MCNP plots are truncated for easier visualization however all the ratio values were calculated with more accuracy. Ratio values less than 1.0 have been italicized for easier comprehension in a grayscale print.

Because of the huge drop off away from the target area, evident in Figs. 3 and 4, this additional dose to adjacent areas could significantly skew the result; the resulting loss of dose in the center region would be trivial given the total dose in the region. This deviation likely only effects analysis close to the target area near the huge slope of the dose profile. Elimination of this source of error would require improved film analysis techniques beyond the current manufacturer recommended protocol.

Another trend observed in comparing scattering behavior in the dose maps of Figs. 5 and 6 is the increase in the ratio of film results to MCNP results at the corners. It is likely that these values are artificially inflated because the film is at the lower limits of its range and therefore reading values skewed high. This effect is most pronounced in the baseline experiment with the 3×3 mm collimator, where the corner doses are very low in the MCNP results and the film results are not able to accurately report values that low. The 5×5 mm collimator results have higher scattering at the corners and therefore avoid hitting the limits of the film measurement range. Future studies could show more details in these low dose regions by using optically stimulated luminescence (OSL) films fabricated with $\text{Al}_2\text{O}_3:\text{C}$, which have been shown to have a minimum detectable dose of <0.5 mGy with the dynamic range extending up to 30 Gy (41).

Comparing the scattered dose in the phantoms versus scattered dose in the baseline experiments does indicate higher levels of scattering within the phantoms; this is expected due to the complex anatomical structures. Scattering levels in the lung irradiation appear lower than those seen in the abdominal irradiation in both the film measurements and the MCNP results. The higher scattering in the abdominal irradiation is likely due to larger amount of higher density material in the path of the beam, i.e., relatively dense tissue versus lower density lung.

Sources of error in our results include the accuracy and uncertainty of simply measuring Gafchromic EBT3 film response with a scanner which was shown to be 1.6% (42). Additionally, the manufacturer advertises uniformity errors, which affect the film response, of $\pm 2\%$ across an $8'' \times 10''$ sheet of Gafchromic EBT3. Statistical errors are also inherent to our MCNP simulations. Our simulations all achieved relative error values of less than 0.05 which is generally reliable yet still a source of uncertainty. Simulations with a goal of reducing error values or increasing the spatial resolution would require significant increases in computational time, especially in areas with low doses. Our comparison of film results and simulation results also presents sources of error due to inaccuracies in replicating the precise physical experiment in the simulation, such as phantom irregularities due to fabrication constraints and alignment of the film to the analysis grid.

These phantoms are unique tools for radiation dosimetry because of their heterogeneous structure, with bone, lung and tissue of differing effective atomic number (Z). Heterogeneities often challenge dosimetric accuracy, which

is vital to preclinical studies that establish dose-response relationships. Megavoltage photon beams used in human radiotherapy are dominated by Compton scattering, whereas the photoelectric effect is dominant in the lower energies such as those produced by the SARRP. The photoelectric effect, which has a strong Z dependence and thus is important in our heterogeneous phantoms, ejects electrons into surrounding matter but for only a relatively short distance (43). Dose contributions from the photoelectric effect are not captured well with EBT3 film because the active region is covered by $125 \mu\text{m}$ of polyester on either side. Future studies utilizing our phantoms along with a radiochromic film with an exposed active region could capture these interactions and provide further insight into dosimetry in small animal models.

Overall the presented studies exhibit the utility of our newly fabricated mouse phantoms for scattered dose measurements. The agreement between our simulated and experimental results using our phantoms are very good, with mean errors of only 9.8% and 18.9% for the 3×3 mm and 5×5 mm collimators, respectively, even though these values are skewed due to outlying high values caused by minor misalignments. Our results support the use of our mouse phantoms in complex irradiation conditions that would be extremely difficult to model, either due to complex irradiation geometry, uncertainty in source specifications, or other complications. Furthermore, a single mouse phantom can be used along with film to gather data from a number of different exposures very quickly. Thanks to the quick processing time of radiochromic film, the results from film irradiations can be viewed within minutes. This is a significant improvement over MCNP calculations which can take days of computational time as well as significant expertise in model programming to obtain a result. Finally, the mouse phantoms are especially useful for experimental conditions with low frequencies of events, such as the scattered dose experiments presented here. Rare events are difficult to obtain significant statistical merit from and thus require extremely long computations. Likewise, locating rare events happening in a small volume is increasingly difficult; experimental results can more easily gather large amounts of data at a high spatial resolution. Using mouse phantoms to experimentally examine these conditions is invaluable in characterizing small animal irradiations.

CONCLUSIONS

The mouse phantoms we have constructed and tested are the most accurate models for radiation dosimetry studies to date. This new generation of phantoms, and more generally the methodology to construct small animal phantoms, will be useful in numerous experiments involving small animal irradiators. As an example of the utility of these phantoms we demonstrated good agreement of measured and simulated values of scattered dose. We believe phantoms such as these will continue to play an important role in verification of small

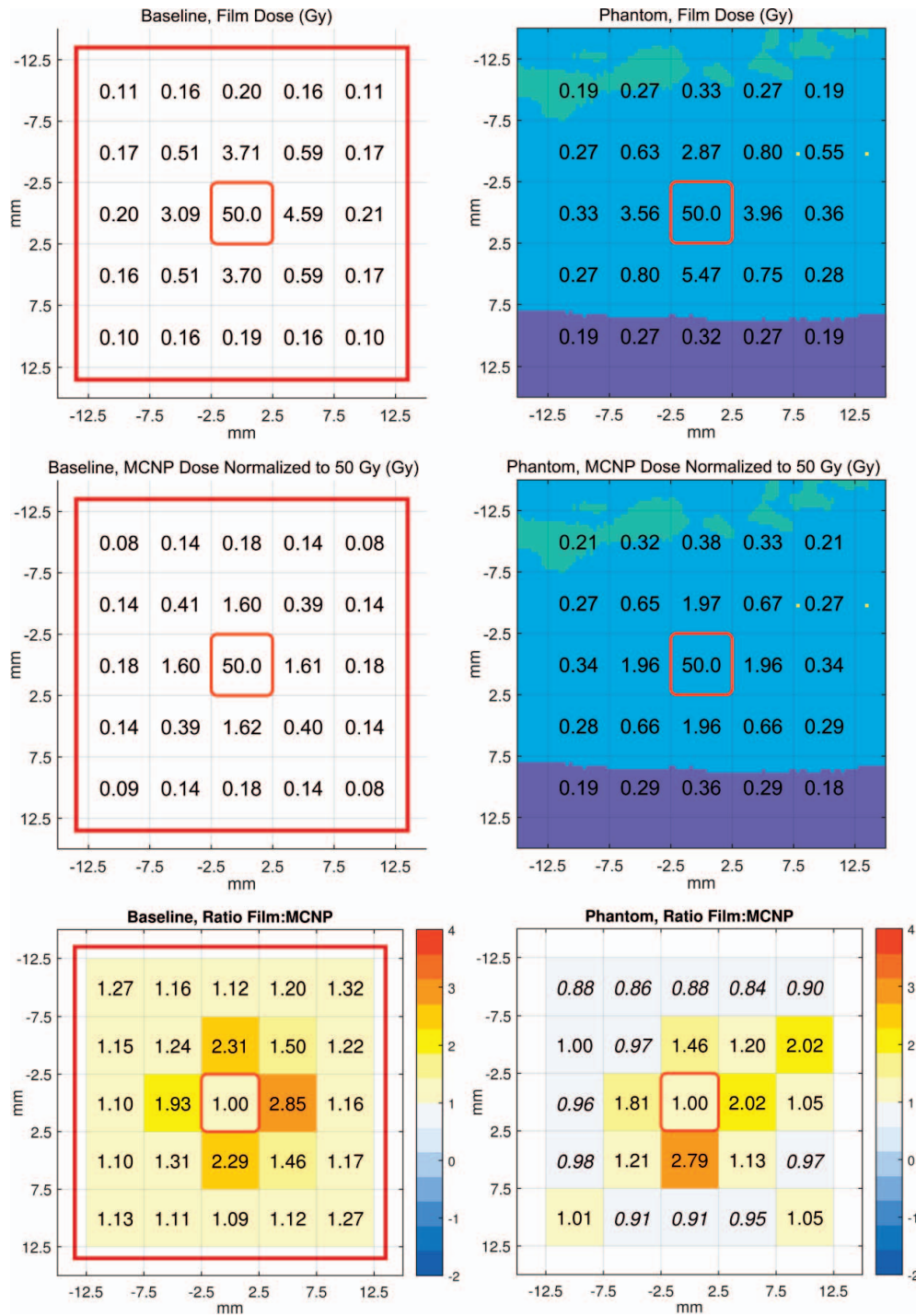


FIG. 6. Plots in the first two rows show dose maps for exposures using the 5×5 mm collimator with film results and MCNP results for both a baseline experiment and a phantom irradiation. Dose is shown normalized to a 50 Gy nominal dose delivered at the center of the beam. The 5×5 mm region highlighted at the center indicates the beam target area. The dose map for the phantom irradiations includes an underlay of the sagittal sliced phantom geometry with bone indicated as gray, tissue as light blue, and air as dark blue. The dose administered to the mouse phantom by the SARRP was aimed at the center of the abdomen and delivered through the side. The bottom two plots show the ratio of film dose to MCNP dose in each of the experimental setups. Values displayed in the film and MCNP plots are truncated for easier visualization however all the ratio values were calculated with more accuracy. Ratio values less than 1.0 have been italicized for easier comprehension in a grayscale print.

animal irradiation systems and confirmation of increasingly complex computational models.

ACKNOWLEDGMENTS

The authors would like to thank Christopher Damoci for his assistance in CT data acquisition at the Herbert Irving Comprehensive Cancer Center Small Animal Imaging Shared Resource facility, Gary Johnson at the Center for Radiological Research for manufacturing the tissue equivalent support rods and Victor Alves at the Brazilian National Cancer Institute for sharing the film2dose program used for film dosimetry. This work was supported by grant number U19-AI067773 to the Center for High-Throughput Minimally Invasive Radiation Biodosimetry from the National Institute of Allergy and Infectious Diseases (NIAID) National Institutes of Health (NIH). The content is solely the responsibility of the authors and does not necessarily represent the official views of the NIAID or NIH.

Accepted: January 15, 2017; published online: January 31, 2017

REFERENCES

- Williams JP, Brown SL, Georges GE, Hauer-Jensen M, Hill RP, Huser AK, et al. Animal models for medical countermeasures to radiation exposure. *Radiat Res* 2010; 173:557–78.
- Verhaegen F, Granton P, Tryggestad E, Small animal radiotherapy research platforms. *Phys Med Biol* 2011; 56:R55.
- Tillner F, Thute P, Löck S, Dietrich A, Fursov A, Haase R, et al. Precise image-guided irradiation of small animals: a flexible non-profit platform. *Phys Med Biol* 2016; 61:3084.
- Tillner F, Thute P, Bütof R, Krause M, Enghardt W, Pre-clinical research in small animals using radiotherapy technology – a bidirectional translational approach. *Zeitschrift für Medizinische Physik* 2014; 24:335–51.
- Yoshizumi T, Brady SL, Robbins ME, Bourland JD, Specific issues in small animal dosimetry and irradiator calibration. *Int J Radiat Biol* 2011; 87:1001–10.
- Kazi AM, MacVittie TJ, Lasio G, Lu W, Prado KL, The MCART Radiation Physics Core: The Quest for Radiation Dosimetry Standardization. *Health Phys* 2014; 106:97–105.
- Knoll GF, *Radiation Detection and Measurement*: John Wiley & Sons; 2010.
- Xu XG, An exponential growth of computational phantom research in radiation protection, imaging, and radiotherapy: a review of the fifty-year history. *Phys Med Biol* 2014; 59:R233.
- Edmond Hui T, Fisher DR, Kuhn JA, Williams LE, Nourigat C, Badger CC, et al. A mouse model for calculating cross-organ beta doses from yttrium-90-labeled immunoconjugates. *Cancer* 1994; 73:951–57.
- Flynn AA, Green AJ, Pedley RB, Boxer GM, Boden R, Begent RHJ, A Mouse Model for calculating the absorbed beta-particle dose from ¹³¹I- and ⁹⁰Y-labeled immunoconjugates, including a method for dealing with heterogeneity in kidney and tumor. *Radiat Res* 2001; 156:28–35.
- Segars WP, Tsui BMW, Frey EC, Johnson GA, Berr SS, Development of a 4-D digital mouse phantom for molecular imaging research. *Mol Imaging Biol* 2004; 6:149–59.
- Taschereau R, Chow PL, Chatziioannou AF, Monte Carlo simulations of dose from microCT imaging procedures in a realistic mouse phantom. *Med Phys* 2006; 33:216–24.
- Taschereau R, Chatziioannou AF, Monte Carlo simulations of absorbed dose in a mouse phantom from 18-fluorine compounds. *Med Phys* 2007; 34:1026–36.
- Larsson E, Strand S-E, Ljungberg M, Jönsson B-A, Mouse S-factors based on Monte Carlo simulations in the anatomical realistic Moby phantom for internal dosimetry. *Cancer Biother Radiopharm* 2007; 22:438–42.
- Stabin MG, Peterson TE, Holburn GE, Emmons MA, Voxel-Based Mouse and Rat Models for Internal Dose Calculations. *J Nucl Med* 2006; 47:655–59.
- Einstein AJ, Elliston CD, Arai AE, Chen MY, Mather R, Pearson GD, et al. radiation dose from single- heartbeat coronary CT angiography performed with a 320-detector row volume scanner 1. *Radiology* 2010; 254:698–706.
- Einstein A, Elliston C, Groves D, Cheng B, Wolff S, Pearson GN, et al. Effect of bismuth breast shielding on radiation dose and image quality in coronary CT angiography. *J Nucl Cardiol* 2012; 19:100–08.
- Archer BR, Glaze S, North LB, Bushong SC, Dosimeter placement in the Rando phantom. *Med Phys* 1977; 4:315–18.
- Sandison GA, Papiez E, Bloch C, Morphis J, Phantom assessment of lung dose from proton arc therapy. *Int J Radiat Oncol Biol Phys* 1997; 38:891–97.
- McDermott L, Perkins A, Comparison of measured and calculated radiotherapy doses in the chest region of an inhomogeneous humanoid phantom. *Australas Phys Eng Sci Med* 2004; 27:16–21.
- Pedersen KH, Kunugi KA, Hammer CG, Culbertson WS, DeWerd LA, Radiation biology irradiator dose verification survey. *Radiat Res* 2016; 185:163–68.
- Perks JR, Lucero S, Monjazeb AM, Li JJ, Anthropomorphic phantoms for confirmation of linear accelerator-based small animal irradiation. *Cureus* 2015; 7:e254.
- Diep P, Pannem S, Sweer J, Lo J, Snyder M, Stueber G, et al. Three-dimensional printed optical phantoms with customized absorption and scattering properties. *Biomed Opt Express* 2015; 6:4212–20.
- Bentz BZ, Chavan AV, Lin D, Tsai EHR, Webb KJ, Fabrication and application of heterogeneous printed mouse phantoms for whole animal optical imaging. *Appl Opt* 2016; 55:280–87.
- Bache ST, Juang T, Belley MD, Koontz BF, Adamovics J, Yoshizumi TT, et al. Investigating the accuracy of micro-stereotactic-body-radiotherapy utilizing anatomically accurate 3D printed rodent-morphic dosimeters. *Med Phys* 2015; 42:846–55.
- Welch D, Harken AD, Randers-Pehrson G, Brenner DJ, Construction of mouse phantoms from segmented CT scan data for radiation dosimetry studies. *Phys Med Biol* 2015; 60:3589.
- Tryggestad E, Armour M, Iordachita I, Verhaegen F, Wong JW, A comprehensive system for dosimetric commissioning and Monte Carlo validation for the small animal radiation research platform. *Phys Med Biol* 2009; 54:5341.
- Chow JCL, Leung MKK, Lindsay PE, Jaffray DA, Dosimetric variation due to the photon beam energy in the small-animal irradiation: A Monte Carlo study. *Med Phys* 2010; 37:5322–29.
- Bazalova M, Graves EE, The importance of tissue segmentation for dose calculations for kilovoltage radiation therapy. *Med Phys* 2011; 38:3039–49.
- Bazalova M, Nelson G, Noll JM, Graves EE, Modality comparison for small animal radiotherapy: A simulation study. *Med Phys* 2014; 41:011710.
- Noblet C, Chiavassa S, Smekens F, Sarrut D, Passal V, Suhard J, et al. Validation of fast Monte Carlo dose calculation in small animal radiotherapy with EBT3 radiochromic films. *Phys Med Biol* 2016; 61:3521.
- Dogdas B, Stout D, Chatziioannou AF, Leahy RM, Digimouse: a 3D whole body mouse atlas from CT and cryosection data. *Phys Med Biol* 2007; 52:577–87.
- Jones AK, Hintenlang DE, Bolch WE, Tissue-equivalent materials for construction of tomographic dosimetry phantoms in pediatric radiology. *Med Phys* 2003; 30:2072–81.
- Winslow JF, Hyer DE, Fisher RF, Tien CJ, Hintenlang DE, Construction of anthropomorphic phantoms for use in dosimetry studies. *J Appl Clin Med Phys* 2009; 10:2986.
- Wong J, Armour E, Kazanzides P, Iordachita I, Tryggestad E, Deng H, et al. high-resolution, small animal radiation research

- platform with x-ray tomographic guidance capabilities. *Int J Radiat Oncol Biol Phys* 2008; 71:1591–99.
36. Lewis D, Micke A, Yu X, Chan MF, An efficient protocol for radiochromic film dosimetry combining calibration and measurement in a single scan. *Med Phys* 2012; 39:6339–50.
37. Alves VGL, Cardoso SC, da Silva AX, Gafchromic EBT2 dosimetry via robust optimization. *Computer Physics Communications* 2013; 184:1708–16.
38. Micke A, Lewis DF, Yu X, Multichannel film dosimetry with nonuniformity correction. *Med Phys* 2011; 38:2523–34.
39. Goorley JT, James M, Booth T, Brown F, Bull J, Cox LJ, et al. Initial MCNP6 release overview-MCNP6 version 1.0. Los Alamos National Laboratory, Los Alamos, NM, LA-UR-13-22934 2013; 1. (<http://bit.ly/2jgY5Wf>)
40. Poludniowski G, Landry G, DeBlois F, Evans PM, Verhaegen F, SpekCalc: a program to calculate photon spectra from tungsten anode x-ray tubes. *Phys Med Biol* 2009; 54:N433.
41. Ahmed MF, Shrestha N, Schnell E, Ahmad S, Akselrod MS, Yukihiro EG, Characterization of Al₂O₃ optically stimulated luminescence films for 2D dosimetry using a 6 MV photon beam. *Phys Med Biol* 2016; 61:7551.
42. Mária M, Benjamin A, Oliver J, Analysis of uncertainties in Gafchromic® EBT film dosimetry of photon beams. *Phys Med Biol* 2008; 53:7013.
43. Johns HE, *Physics of Radiology*: Charles River Media; 1983.